Title

Contactless Suspension of a Silicon Disk

Authors

Pyle, Kenneth E

M'Closkey, Robert T

Publication Date

2023

Contactless Suspension of a Silicon Disk

Kenneth E. Pyle[1] and Robert T. M'Closkey[2]

Abstract— **A system to suspend a silicon disk between two sets of stator electrodes is reported. Electrode pairs are used for both control and sensing by exerting electrostatic forces on the disk and measuring differential capacitances related to the disk's position. The disk is a six degree-of-freedom system, however, lateral and yaw motion are not measurable by the electrode arrangement so only the disk's vertical position, roll, and pitch are regulated. Two separate control strategies are pursued –decentralized feedback around the electrode-disk gaps and feedback around a decoupled coordinate frame related to the disk's controllable degrees-of-freedom. Experimental frequency responses obtained from closed-loop results of the suspended disk are reported and compared to analytical models.**

I. INTRODUCTION

The electrostatic suspension of a thin silicon disk between two sets of electrodes is reported. This system is under development to remove substrate coupling when testing micro-scale resonators. The rigid disk has six degrees-of-freedom, however, only the vertical and two out-of-plane rotational degrees-of-freedom are observable with the electrode arrangement shown in Fig. 1. Lateral translational motion is passively stabilized by fringe field forces since the radius of the disk matches the outer radius of the electrodes. The same electrodes exert electrostatic control forces and quantify the disk position by measuring differential capacitances. Using the same electrodes for both sensing and control reduces the voltage amplitude required to suspend the disk so that electrical arcing is not a concern. This modality produces significant "feedthrough" from the control signal to the electronic pickoffs and must be removed from the measurements prior to implementing the feedback controller.

The dual function of the electrodes is achieved using transformers in the same manner as that proposed for an electrostatic bearing that supports a gyroscope rotor in [1], [2]. Alternative transduction schemes for the electrostatic suspension of disks and spheres has been proposed for a variety of systems including inertial sensors, material handling systems, and media storage in [3]–[7]. Electrostatic levitation of a square glass plate and a thin ring have been described in [8] and [9], respectively, however, separate instruments are used for control and detection. The disk-electrode arrangement and electronics herein are similar to those reported in [10], however, in the present work the disk diameter is equal to the electrode footprint. Consequently, the lateral position cannot be controlled but is passively stabilized by the lateral forces produced by the fringe field created between the electrodes and disk. Additional electrodes are used to detect and specify lateral displacements in [10], however, that system is unable to hold non-zero disk angles. The three degree-of-freedom system discussed here is capable of specifying out-of-plane rotational motion of the disk. Since the same transducers are used in both studies, the simplified system reported herein is designed to provide insight into non-idealities in the transformers, a decoupling procedure that takes into account differences in the transduction gains, and changes in the feedthrough as the nominal setpoint of the disk varies. These insights are intended to improve the modeling and control of the five degree-of-freedom disk in [10] so that the system can be miniaturized to suit micro-scale systems.

II. SYSTEM DESCRIPTION

The 7.4 cm diameter, 400 μm thick disk is etched from a silicon wafer and sputtered with aluminum. Two identical sets of electrodes –a top set and a bottom set –are used to suspend the disk, as shown in Fig. 1. Each set is patterned on a glass plate and the plates are oriented parallel to one another such that the top and bottom electrodes are mirror images of each other. The electrode sets are arranged in pie-shaped formations with each set consisting of four equally sized electrodes having an area of 10.3 cm^2. The electrodes are grouped into four pairs of facing electrodes, i.e. electrodes $\mathcal{E}_{\mathrm{t}_k}$ and $\mathcal{E}_{\mathrm{b}_k}$, $k = 1, 2, 3, 4$, are grouped into a pair. Each pair is used for two purposes –to exert electrostatic control forces on the disk and to measure the differential electrode-disk capacitances that are used to sense the disk's position. This electrode configuration provides measurements of the vertical and two tilt degrees-of-freedom. Lateral motion and yaw rotation are not observable and the disk's lateral motion is passively stabilized by fringe field forces since the outer radius of the electrodes matches the radius of the disk. The gap between the upper and lower glass plates is set using precision shims and silicon spacers that are etched from the same wafer as the disk. When the disk is perfectly centered between the electrodes, the vertical gap between the disk and each electrode is 134 μm. A thin layer of photoresist coats each of the glass plates to ensure that the disk never has direct contact with the electrodes.

Transformers are used to pair the top and bottom electrodes, as shown in Fig. 2. One transformer is used per electrode pair and each of the electrodes within a given pair is connected to one of its transformer's primary leads. The transformers are supplied with a constant amplitude, 25 kHz sinusoidal center tap and the primary inductances

[1]Kenneth E. Pyle is a Graduate Student Researcher in the Mechanical and Aerospace Engineering Department, University of California, Los Angeles, CA 90095 USA kennypyle@ucla.edu.

[2]Robert T. M'Closkey is corresponding author and Professor of Mechanical and Aerospace Engineering, University of California, Los Angeles, CA 90095 USA rtm@seas.ucla.edu.

are identical on either side of the center tap. Two additional transformers are used to supply the center tap currents. The primary leads of each of these additional transformers are connected to the center taps of two adjacent "electrode" transformers so that equal and opposite currents are supplied to the center taps. This ensures that any positive charge added to the disk by one electrode set is removed by an adjacent electrode set. Since the disk is established at ground potential before any electronics are turned on, supplying the center taps in this fashion ensures that it remains at ground potential, even when suspended. By configuring the transformers in this manner, any deviation between the top and bottom capacitances within an electrode pair, C_{t_k} and C_{b_k}, respectively, creates a nonzero voltage drop across the transformer secondary, v_{s_k}. The amplitude of this voltage drop is proportional to the degree of asymmetry in the capacitances and is used as a measure of the disk's vertical position relative to the centroids of the electrodes within a given pair. This measurement establishes a convenient null position of the disk. When the disk is perfectly centered between the electrodes, the capacitances between the disk and the top electrodes are equivalent to the capacitances between the disk and the bottom electrodes (about 77 pF). This produces identical voltages on the top and bottom electrodes such that zero voltage drop occurs across the transformer secondary.

The same transformers used for sensing are also used to exert electrostatic control forces on the disk by a control voltage, v_{c_k}, that is added in parallel to the transformer secondary via resistor R_{c}. The control voltage is modulated to operate at the same 25 kHz frequency as the center tap and the modulation phase, ϕ_{c_k}, is set to maximize the voltage differential created between the top and bottom electrodes when v_{c_k} is nonzero. This voltage differential is established by the fact that a nonzero control voltage creates sinusoidal voltage components on the top and bottom electrodes that are in anti-phase with one another. This is in contrast to the center tap, which produces sinusoidal voltages on both the top and bottom electrodes that are in-phase with each other. The net voltages on the electrodes are sinusoidal with a frequency of 25 kHz and an amplitude based on the superposition of the the center tap- and control-induced voltages. The electrostatic forces exerted on the disk are proportional to the square of the electrode voltages, however, the disk's inertia acts as a low-pass filter such that the disk essentially responds to the mean-square value of the electrode voltages. Using the same transformers for both sensing and control presents a significant amount of feedthrough from v_{c_k} to v_{s_k}, i.e. even if the disk position remains fixed, an adjustment in v_{c_k} changes the amplitude of v_{s_k}. Accurate cancellation of this feedthrough is required in order to suspend the disk.

The plant inputs, u_k's, and outputs, ζ_k's, are baseband signals that are generated and sampled by a digital signal processor operating at 5 kHz. The DSP is used to implement the digital feedback controllers, feedforward filter, and coordinate transformation discussed in the following sections. All modulation of the control signals and demodulation of the sense signals is performed using analog electronics. The demodulation phases are selected such that the demodulation carrier is in-phase with v_{s_k}. Additionally, analog Butterworth filters are used to smooth the output signals of the DSP and for anti-aliasing. A schematic of a single input/output channel of the plant is provided in Fig. 2.

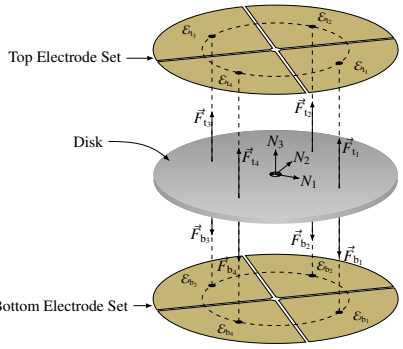

Fig. 1: Exploded view of the disk and electrodes.

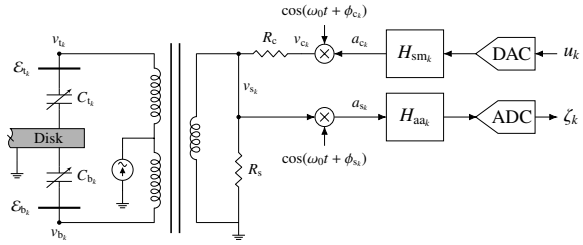

Fig. 2: Schematic of a single input/output channel of the plant consisting of the smoothing filter, H_{sm_k}, analog modulator, transformer-disk subsystem, analog demodulator, and anti-alias filter, H_{aa_k}.

III. SYSTEM MODEL

The disk dynamics are defined according to the generalized coordinates $q = [x, y, z, \theta, \varphi]^T$ where $\{x, y, z\}$ represent translations of the disk center of mass relative to the N_1, N_2, and N_3 axes of the fixed N-frame, respectively, and θ, φ represent an Euler angle sequence about the N_1 and B_2 axes (see Fig. 3). The inertial N-frame has its origin defined at the geometric center of the electrode configuration, with the N_1 and N_2 axes extending parallel to the electrodes and the N_3 axis piercing the center of the top electrode set. The disk-fixed B-frame is defined by an origin at the disk's center of mass, B_1 and B_2 axes that lie within the plane of the disk, and a B_3 axis that points normal to the disk. When the disk configuration is such that $q = 0$, the N- and B-frames are coincident. Rotation about the vertical axis is neglected in the model since it has no impact on the equations of motion and it is not possible to spin the disk about this axis using the electrode arrangement shown in Fig. 1.

The disk and electrodes are modeled as parallel plate capacitors due to the disk-glass plate geometry that constrains any rotation of the disk to less than 4 mrad. The deflection of the disk is measured along lines interpolating the geometric

centroids of each electrode within a pair. Using the small angle approximation, the vertical deflection of the disk from the origin of the N-frame along the centroid-interpolating lines is given by

$$z_k = z + (x - \bar{x}_k)\varphi + (\bar{y}_k - y)\theta \quad k = 1, 2, 3, 4 \tag{1}$$

where $(\bar{x}_k, \bar{y}_k)$ is the lateral position of each electrode pair's centroid in the N-frame. These vertical displacements are used to compute the effective disk-electrode gaps of the parallel plate capacitor model and, in conjunction with the electrode centroids, to define the position of the effective electrostatic point forces that act on the disk. Assuming that the disk is at ground potential, the electrostatic point forces are oriented normal to the disk with magnitudes given by

$$\begin{aligned} F_{\mathrm{t}_k} &= \frac{\epsilon_0 \epsilon_r A_e}{2(z_0 - z_k)^2} v_{\mathrm{t}_k}^2 \\ F_{\mathrm{b}_k} &= \frac{\epsilon_0 \epsilon_r A_e}{2(z_0 + z_k)^2} v_{\mathrm{b}_k}^2, \end{aligned} \qquad k = 1, 2, 3, 4 \tag{2}$$

where A_e represents the electrode area and z_0 is the nominal electrode-disk gap.

Gravitational, squeeze film damping, and fringe field effects are also considered in the model. The squeeze film damping forces and moments are proportional to the vertical and angular velocities, respectively, and are computed from [11]. The net fringe field forces are modeled as linear springs that passively center the disk within the N_1-N_2 plane. These forces, denoted by F_x and F_y in Fig. 3, are assumed to be proportional to small lateral displacements of the disk and a spring rate, k_s, is estimated so that the lateral modes have a 1 Hz resonance. Computing the generalized forces associated with q using the small angle approximation yields

$$\begin{aligned} m\ddot{x} &= \varphi \sum_{k=1}^{4} F_k - k_s x, \quad m\ddot{y} = -\theta \sum_{k=1}^{4} F_k - k_s y \\ m\ddot{z} &= \sum_{k=1}^{4} F_k - mg - c_z \dot{z}, \quad J_t \ddot{\theta} = \sum_{k=1}^{4} (\bar{y}_k - y) F_k - c_\theta \dot{\theta} \\ J_t \ddot{\varphi} &= \sum_{k=1}^{4} (x - \bar{x}_k) F_k - c_\varphi \dot{\varphi}, \end{aligned}$$

where m and J_t are the disk mass and transverse axis moment of inertia, respectively, $\{c_z, c_\theta, c_\varphi\}$ represent the squeeze film damping coefficients, and $F_k = F_{\mathrm{t}_k} - F_{\mathrm{b}_k}$. The linearized disk equations of motion can be expressed as a set of coupled first order differential equations

$$\frac{d}{dt}\begin{bmatrix} q \\ \dot{q} \end{bmatrix} = \begin{bmatrix} \dot{q} \\ f(q, \dot{q}, w_{\mathrm{t}}) \end{bmatrix} \tag{3}$$

where w_{t} is the state vector that describes the transformer dynamics. The transformer dynamics have been investigated in detail in [12], [13] and the equations of motion are given as

$$\begin{aligned} M(q)\dot{w}_{\mathrm{t}} &= A w_{\mathrm{t}} + B_1 i_{\mathrm{ct}} + B_2 v_{\mathrm{c}} \\ v_{\mathrm{s}} &= C w_{\mathrm{t}} \end{aligned} \tag{4}$$

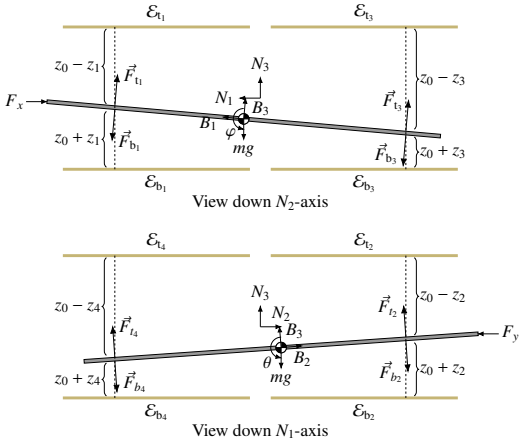

Fig. 3: Side view of the disk and electrodes (not to scale).

where i_{ct} is the current source at the transformer center tap, $v_{\mathrm{c}} = [v_{\mathrm{c}_1}, v_{\mathrm{c}_2}, v_{\mathrm{c}_3}, v_{\mathrm{c}_4}]^T$ is the vector of control voltages, and $v_{\mathrm{s}} = [v_{\mathrm{s}_1}, v_{\mathrm{s}_2}, v_{\mathrm{s}_3}, v_{\mathrm{s}_4}]^T$ is the vector of sense voltages. The electrode-disk capacitances that are a function of the disk position are contained in the mass matrix, $M(q)$.

The analog modulators/demodulators and Butterworth filters pictured in Fig. 2 contribute additional states to the plant model. The input electronics are described by

$$\begin{aligned} \dot{w}_{\mathrm{sm}} &= A_{\mathrm{sm}} w_{\mathrm{sm}} + B_{\mathrm{sm}} u \\ v_{\mathrm{c}} &= \mathcal{C}_{\mathrm{c}} C_{\mathrm{sm}} w_{\mathrm{sm}} \end{aligned} \tag{5}$$

where $\mathcal{C}_{\mathrm{c}} = \mathrm{diag}(\cos(\omega_0 t + \phi_{\mathrm{c}_1}), ..., \cos(\omega_0 t + \phi_{\mathrm{c}_4}))$ is the diagonal matrix of sinusoids representing the analog modulators and $(A_{\mathrm{sm}}, B_{\mathrm{sm}}, C_{\mathrm{sm}}, 0)$ characterizes the state-space model for the smoothing filters with state vector w_{sm}. Similarly, the sensing electronics are characterized by

$$\begin{aligned} \dot{w}_{\mathrm{aa}} &= A_{\mathrm{aa}} w_{\mathrm{aa}} + B_{\mathrm{aa}} \mathcal{C}_{\mathrm{s}} v_{\mathrm{s}} \\ \zeta &= C_{\mathrm{aa}} w_{\mathrm{aa}} \end{aligned} \tag{6}$$

where $\mathcal{C}_{\mathrm{s}} = \mathrm{diag}(\cos(\omega_0 t + \phi_{\mathrm{s}_1}), ..., \cos(\omega_0 t + \phi_{\mathrm{s}_4}))$ is the diagonal matrix representing the analog demodulators and $(A_{\mathrm{aa}}, B_{\mathrm{aa}}, C_{\mathrm{aa}}, 0)$ describes the state-space representation for the anti-alias filters with state vector w_{aa}. The coupled plant dynamics are collectively governed by (3)-(6).

A periodic solution of the coupled nonlinear system can be generated with the disk suspended at its equilibrium position ($q = \dot{q} = 0$). Such a solution exists when the mean value of all forces and moments acting on the disk sum to zero and the control input is appropriately chosen to counteract the gravitational force acting on the disk. Linear variational equations are computed about this equilibrium condition by introducing perturbation variables: $u = \bar{u} + \delta_u$, $w_{\mathrm{t}} = \bar{w}_{\mathrm{t}} + \delta_{w_{\mathrm{t}}}$, and so forth, where the bar notation is used to define the states at the equilibrium condition. Collecting all of the perturbation state variables in δ, the linear variational equations yield a time periodic model represented by

$$\begin{aligned} \dot{\delta} &= A_\delta \delta + B_\delta \delta_u \\ \delta_\zeta &= C_\delta \delta. \end{aligned} \tag{7}$$

The solution to an initial value problem posed by (7) is given by

$$\delta(t) = \Theta(t, t_0)\delta(t_0) + \int_{t_0}^{t} \Theta(t, \tau) B_\delta(\tau)\delta_u(\tau) d\tau, \;\; t \geq t_0$$

where $\Theta(t, t_0)$ is the state transition matrix from time t_0 to time t associated with (7). The start time specifies the phase of the time-varying periodic solution, though it is well documented in [12] that it has negligible effect on the model when viewed from a frequency domain perspective, thus t_0 will be assumed to be zero for the remaining analysis.

A discretized time-invariant model can be developed using the fact that the sinusoidal carrier operates at a frequency that is an integer multiple of the DSP sample rate. Viewing the initial value problem from the lens of successive samples at the DSP sample rate yields

$$\begin{aligned}\delta((l+1)t_s) = \Theta((l+1)t_s, lt_s)\delta(lt_s) \\ + \int_{lt_s}^{(l+1)t_s} \Theta((l+1)t_s, \tau) B_\delta(\tau)\delta_u(\tau) d\tau,\end{aligned} \tag{8}$$

where l is the sample index integer. Due to the the zero-order hold instituted by the DSP, the input variable, δ_u, is constant over the integration bounds, so the discrete-time state space model can be expressed as

$$\begin{aligned}\delta((l+1)t_s) = \Phi\delta(lt_s) + \Gamma\delta_u(lt_s) \\ \delta_\zeta = C_\delta\delta(lt_s)\end{aligned} \tag{9}$$

where $\Phi = \Theta(t_s, 0)$ and $\Gamma = \int_0^{t_s} \Theta(t_s, \tau) B_\delta(\tau) d\tau$.

Solving the difference equation in (9) yields the four-input/four-output plant model illustrated in Fig. 4. Only one input channel is shown, though the symmetry of the system makes identifying the remaining transfer functions trivial. For instance, the diagonal channels will all be identical. The model contains three unstable eigenvalues with continuous-time approximations of 1.14, 1.56, and 1.56 Hz. The 1 Hz notch present in the diagonal and antipodal (the output channel electrode pair is opposite the input channel electrode pair) channels is the result of the fringe field springs. A high degree of feedthrough coupling occurs in the diagonal channels from using the same electrodes for both sensing and control. This is evident in the dashed purple and blue lines of Fig. 4 that represent the transfer functions in the $(1, 1)$ elements of F and P, respectively. The solid blue trace that indicates the ζ_1/u_1 transfer function is computed by subtracting the dashed purple line from the dashed blue trace. The analytical feedthrough model is estimated by removing the states associated with the disk dynamics from (9). In practice, the feedthrough is mitigated by identifying a feedforward FIR filter with the disk resting at its bottom position.

IV. PRELIMINARY CONTROLLER DESIGN

The multivariable feedback loop is provided in Fig. 5, where $r, u, \zeta \in \mathbb{R}^4$, G is the feedback controller, and F represents the feedforward FIR filter. SISO feedback controllers are designed around the diagonal channels of the plant in

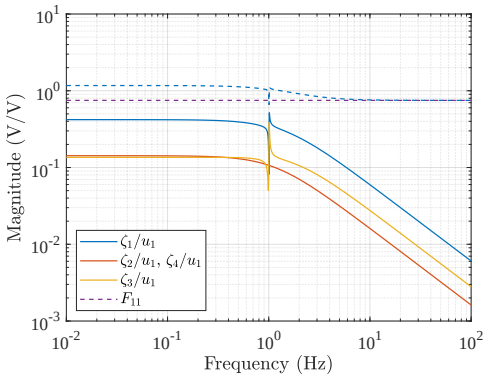

Fig. 4: Analytical frequency responses of the four plant outputs to input channel u_1. The dashed blue trace indicates the ζ_1/u_1 transfer function in the absence of feedthrough cancellation. The effect of the lightly damped lateral modes is visible in a neighborhood of 1 Hz.

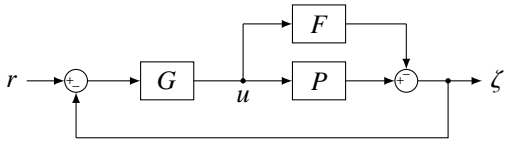

Fig. 5: Closed-loop architecture of the four-input/four-output plant.

order to control each electrode-disk gap. Based on the model, proportional controllers will stabilize the system, however, imperfect cancellation of high frequency feedthrough makes practical suspension more challenging so the controller gain is rolled-off at high frequencies. The SISO controllers are of the form

$$G_k = 8\frac{200\pi}{s + 200\pi}, \quad k = 1, 2, 3, 4 \tag{10}$$

and analysis of the closed-loop eigenvalues indicates nominal stability since the real part of each eigenvalue is strictly less than -4 (ignoring those corresponding to the lateral degrees-of-freedom, which lie just inside the open left-half plane). This analysis is repeated for a set of varying fringe field spring stiffnesses and nominal stability of the closed-loop system is maintained so long as the spring rate produces a lateral resonance greater than 0.08 Hz.

Due to the imperfect feedthrough cancellation of the feedforward filter, unstructured additive perturbations are considered around F. While conservative, the H_∞ norm of the pertinent transfer function seen from the perspective of the uncertainty model indicates that perturbations in the feedforward filter of at least 12% are acceptable for maintaining closed-loop stability. It is evident in Fig. 4 that the feedthrough exceeds the magnitude of the transfer functions related to the physical disk dynamics in the diagonal channels. Thus, high fidelity feedthrough cancellation is required for stability and that is reflected in the robustness margins.

The diagonal controller is discretized using Tustin's method and implemented by the DSP. Estimates of the

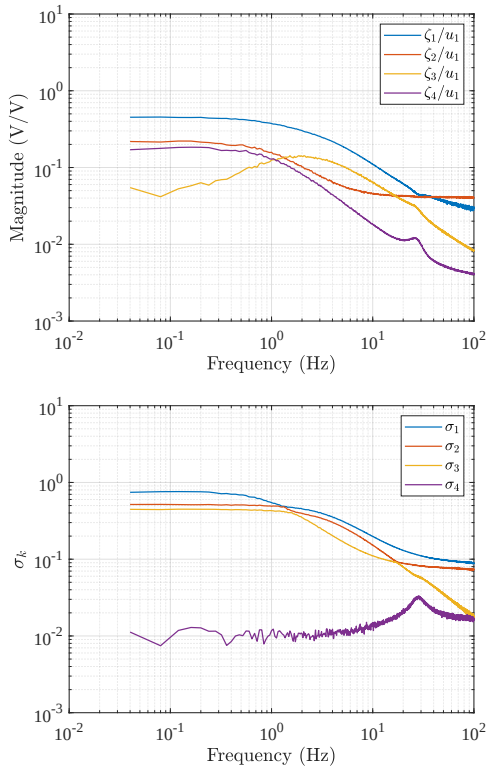

Fig. 6: **Top:** Empirical frequency responses of the plant to a broadband random input at u_1. The remaining three input channels exhibit the same trends. **Bottom:** Singular values of the four-input/four-output empirical plant.

open-loop plant model with the feedthrough removed are obtained from closed-loop measurements of the suspended disk. Standard spectral estimation techniques are employed to gather the u/r and ζ/r transfer functions. The empirical model is generated according to $P - F = \zeta/r \cdot (u/r)^{-1}$ and is plotted in Fig. 6 for input channel u_1. Small differences between input channels are observed due to inconsistencies in the transduction gains, however, for brevity, the frequency responses for the remaining input channels are not plotted. The empirical data indicates that the analytical model developed is fairly accurate in predicting the plant dynamics, especially at low frequencies, however, the lateral modes due to fringe field forces –estimated at 1 Hz in the analytical model –do not appear in any of the channels. Deviation from the expected s^{-1} roll-off above 10 Hz is the result of residual feedthrough. The low DC gain and hump near a couple of Hz in the ζ_3/u_1 transfer function occur in all of the antipodal transfer functions and further investigation of the modeling assumptions are required to understand the plant dynamics in these input/output channels. The singular values of the plant are also plotted versus frequency in Fig. 6 and indicate the dominance of three singular values for frequencies below 10 Hz. This motivates a decoupling procedure for a three-input/three-output plant based on a singular value decomposition of the four-input/four-output plant model.

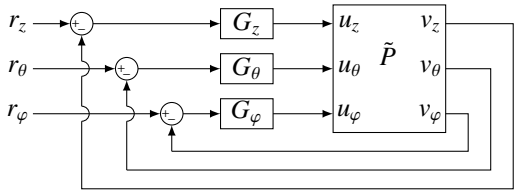

Fig. 7: Closed-loop architecture of the decoupled plant. The decoupling matrices and feedforward filter are lumped into $\tilde{P}$.

V. CONTROL OF THE DECOUPLED PLANT

A decoupling procedure is applied to the four-input/four-output plant so that the inputs and outputs of the plant in the new coordinate frame correlate with the disk's vertical and tilt degrees-of-freedom. A singular value decomposition of $\mathrm{Re}(P) = U\Sigma V^T$ is computed at a frequency of 0.36 Hz, where the phases of all channels of the empirical model are essentially 0° or 180°. The input decoupling matrix, $\mathcal{D}_u$, is taken to be the first three columns of the V matrix and the output decoupling matrix, $\mathcal{D}_\zeta$, is the transpose of the first three columns of U. A new feedforward FIR filter, $\tilde{F}$, can be identified in this new coordinate frame and this filter is lumped into the new plant model, $\tilde{P}$, such that $\tilde{P} = \mathcal{D}_\zeta P \mathcal{D}_u - \tilde{F}$. It is important to note that the decoupling matrices produced by the singular value decomposition define the three degrees-of-freedom in a different coordinate frame than that used in the analytical model derived in Sec. III, nevertheless, alignment of the coordinate frames is a calibration problem that can be resolved using a transformation matrix.

Working in the decoupled coordinate frame has two main benefits: the diagonal channels of the plant are over an order of magnitude larger than the off-diagonal channels, simplifying robust control design, and integrators can be used to position the disk exactly with respect to its vertical and tilt degrees-of-freedom. In the non-decoupled plant, the closed-loop system is not asymptotically stable if an integrator is introduced to each non-zero control element G_k in (10). This is unsurprising since the disk's $\{z, \theta, \varphi\}$ configuration is defined by three points, so an inconsistent specification can be produced by defining four gaps.

In a similar approach to the previous section, SISO controllers are designed around the diagonal elements of the plant as illustrated in Fig. 7. The vertical and tilt controllers are PI controllers with high frequency roll-offs given by

$$G_z = 8\frac{200\pi}{s+200\pi} + \frac{10}{s}, \quad G_\theta = 8\frac{200\pi}{s+200\pi} + \frac{5}{s} \qquad (11)$$

where G_z is the controller around the vertical degree-of-freedom and $G_\theta = G_\varphi$ are the tilt controllers. These three controllers are collectively grouped in the multivariable controller $\tilde{G} = \mathrm{diag}(G_z, G_\theta, G_\varphi)$. Analysis of the Nyquist plot of $\det(I + \tilde{P}\tilde{G})$ indicates nominal stability of the closed-loop system. Unstructured multiplicative perturbations at both the decoupled plant input and output are (separately) considered using the empirical plant model generated in Sec. IV. The

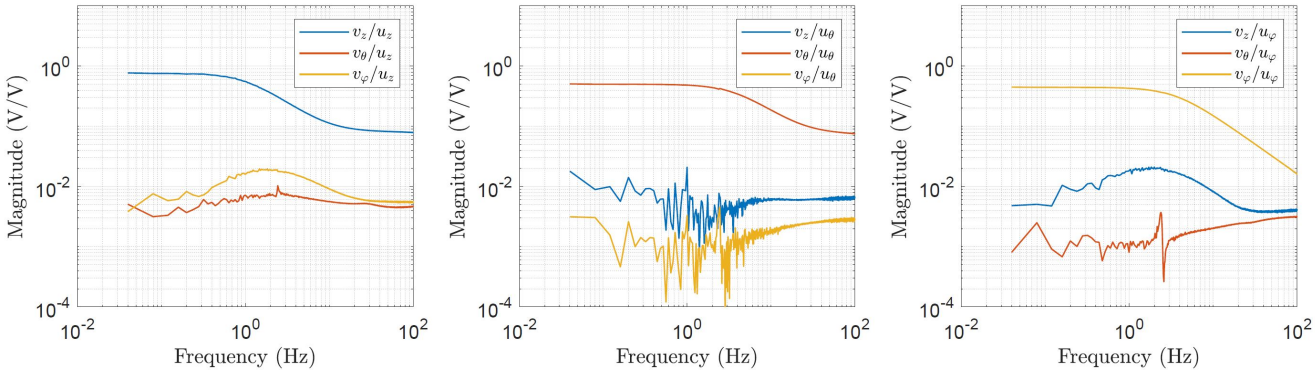

Fig. 8: Empirical frequency responses of the decoupled plant. The lateral resonance due to strong fringe field forces appears in the v_θ/u_z and v_θ/u_φ transfer functions near 2.4 Hz.

H_∞ norm of the input and output complementary sensitivity functions provide conservative metrics that indicate that the closed-loop system is robustly stable to plant uncertainties of at least 30% of the identified plant gain.

Digital implementation of the decoupled plant controller yields the empirical frequency response model of $\tilde{P}$ shown in Fig. 8. This data was also generated from measurements of closed-loop transfer functions using spectral estimation techniques. The lateral spring rate appears in the v_θ channels with a resonance of about 2.4 Hz and residual feedthrough coupling causes the flat magnitude band above 10 Hz in the diagonal channels. The v_φ/u_φ transfer function, however, does appear to show improved feedthrough rejection. The inclusion of integrators in the controller allows similar models to be generated about various N_3-directional setpoints to provide insight into how the feedthrough changes as the nominal disk position varies. Differences between such models indicate that only about an order of magnitude reduction in the feedthrough can be expected using the transduction scheme employed herein since improvements in feedthrough reduction at one setpoint do not correlate with enhanced feedthrough cancellation at another.

In comparison to the disk in [10] that is not passively stabilized in the lateral directions, the disk here can be controlled in the tilt degrees-of-freedom for applications that require it. In [10], any step input to the tilt channels creates a change in the lateral position of the disk, but the steady state angles remain zero. An unstable control law presented additional challenges in that work, especially since the decoupling matrices were developed from the kinematics of the system. Identification of the "true" decoupling matrices that depend on transduction inconsistencies between channels in this system can be extended to that in [10].

VI. CONCLUSION

Electrostatic levitation of a thin disk is achieved via two separate control strategies: low-pass feedback controllers around each of the electrode-disk gaps and PI controllers in a decoupled coordinate frame. This three degree-of-freedom system is designed to provide insight into the decoupling procedure and non-idealities in the control and sensing electronics that can be used in a more complex five degree-of-freedom disk. Residual feedthrough coupling complicates closed-loop suspension of the disk and an alternative electrode arrangement that separates control from sensing electronics will be addressed in future papers.

ACKNOWLEDGEMENT

The authors thank the UCLA Nanoelectronics Research Facility for their assistance fabricating the disk and electrodes. This work was not supported by any organization.

REFERENCES

[1] J. L. Atkinson, "Electrostatic bearing," U.S. Patent 3 334 949, 1967.
[2] ——, "Electrostatic bearing sensing and control circuitry," U.S. Patent 3 891 285, 1975.
[3] J. Jin, T. Higuchi, and M. Kanemoto, "Electrostatic levitator for hard disk media," *IEEE Transactions on Industrial Electronics*, vol. 42, no. 5, pp. 467–473, 1995.
[4] J. Jin, T. C. Yih, T. Higuchi, and J. U. Jeon, "Direct electrostatic levitation and propulsion of silicon wafer," *IEEE Transactions on Industry Applications*, vol. 34, no. 5, pp. 975–984, 1998.
[5] R. Toda, N. Takeda, T. Murakoshi, S. Nakamura, and M. Esashi, "Electrostatically levitated spherical 3-axis accelerometer," in *Technical Digest. MEMS 2002 IEEE International Conference. Fifteenth IEEE International Conference on Micro Electro Mechanical Systems (Cat. No.02CH37266)*, Jan 2002, pp. 710–713.
[6] F. Han, Z. Gao, D. Li, and Y. Wang, "Nonlinear compensation of active electrostatic bearings supporting a spherical rotor," *Sensors and Actuators A: Physical*, vol. 119, no. 1, pp. 177–186, 2005.
[7] E. van West, A. Yamamoto, and H. Toshiro, "Manipulation of thin objects using levitation techniques, tilt control, and haptics," *IEEE Transactions on Automation Science and Engineering*, vol. 7, no. 3, pp. 451–462, 2010.
[8] J. U. Jeon and T. Higuchi, "Electrostatic suspension of dielectrics," *IEEE Transactions on industrial electronics*, vol. 45, no. 6, pp. 938–946, 1998.
[9] T. Murakoshi, Y. Endo, K. Fukatsu, S. Nakamura, and M. Esashi, "Electrostatically levitated ring-shaped rotational-gyro/accelerometer," *Japanese Journal of Applied Physics*, vol. 42, no. Part 1, No. 4B, pp. 2468–2472, 2003.
[10] M. Andonian and R. T. MCloskey, "An electrostatically suspended contactless platform," *Mechatronics*, vol. 80, p. 102685, 2021.
[11] M. Bao and H. Yang, "Squeeze film air damping in mems," *Sensors and Actuators A: Physical*, vol. 136, no. 1, pp. 3–27, 2007.
[12] M. Andonian and R. T. M'Closkey, "Sensing and control interface for precise gap control," *Mechatronics*, vol. 56, pp. 277–286, 2018.
[13] ——, "Identification and compensation of feedthrough in an unstable electrostatic bearing," *Mechatronics*, vol. 65, p. 102315, 2020.